Journal of
Materials Chemistry C

Materials for optical, magnetic and electronic devices

Accepted Manuscript

This article can be cited before page numbers have been issued, to do this please use: I. Silva, N. Pereira, N. Peinka, D. Correia and S. Lanceros-Mendez, *J. Mater. Chem. C*, 2026, DOI: 10.1039/D6TC00186F.

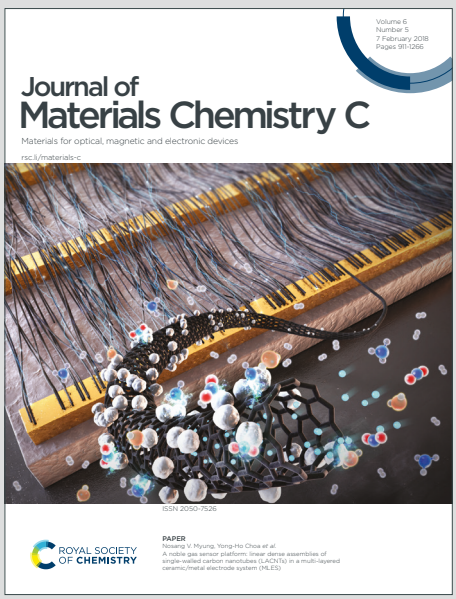

ROYAL SOCIETY OF CHEMISTRY

rsc.li/materials-c

View Article Online
DOI: 10.1039/D6TC00186F

Electrical Double-Layer based Wearable Tensile and Pressure Sensors: Optimizing Materials and Architecture for Improved Sensing Response

I.R.Silva [a], N. Pereira [a,*], N. Perinka[b], D. M. Correia[c], S. Lanceros-Méndez [a,b,d,*]

[a] Physics Centre of Minho and Porto Universities (CF-UM-UP) and Laboratory of Physics for Materials and Emergent Technologies (LapMET), University of Minho 4710-057 Braga, Portugal

[b] BCMaterials, Basque Center for Materials, Applications and Nanostructures, UPV/EHU Science Park, 48940 Leioa, Spain

[c] Centre of Chemistry, University of Minho, 4710-057 Braga, Portugal

[d] Ikerbasque, Basque Foundation for Science, 48009 Bilbao, Spain

* Corresponding Authors

Abstract

The development of wearable electronics requires a higher understanding of the structural parameters that enable selective mechanical sensing across different deformation modes. In this work, we present a materials-to-architecture framework for multifunctional iontronic textile sensors based on thermoplastic polyurethane (TPU) and the ionic liquid (IL) -butyl-3-methylimidazolium thiocyanate [Bmim][SCN]. By systematically incorporate different IL contents from 0 to 60 wt.%, the sample incorporating 40 wt.% displayed the optimal balance between ionic conductivity and long-term environmental stability by preventing IL surface migration. When processed as dense films, the TPU/[Bmim][SCN] (T_{IL}) enables linear strain sensing (S = 0.58). Conversely, the integration of both TPU and IL [Bmim][SCN] into a porous neoprene scaffold (N-T_{IL}) creates an interface that amplifies the effective electrochemical double layer (EDL) effect, yielding a six-fold increase in pressure sensitivity (1.8×10^{-2} kPa^{-1}). Electrochemical impedance spectroscopy (EIS) confirms that the architectural transition from dense to porous reduces interfacial resistance and introduces additional Maxwell–Wagner–Sillars interfaces. A glove prototype was developed to demonstrate the sensor ability to detect joint flexion from fingertip pressure by matching the sensor architecture to the specific stimulus.

View Article Online
DOI: 10.1039/D6TC00186F

Keywords: Wearable textile sensors, capacitive sensing, electrical double layer, ionic liquids, TPU

1. Introduction

Textiles are emerging as the dominant platform for next-generation wearable interfaces, requiring sensors that strictly balance high electromechanical sensitivity with the inherent mechanical compliance of the human body [1-4]. Unlike rigid electronics, smart textiles integrate sensing capabilities directly into the structural hierarchy of textiles, enabling continuous health monitoring and motion tracking without compromising comfort or flexibility. Among the transduction mechanisms employed in these systems, capacitive sensing has been prioritized for its low power consumption, high linearity, and compatibility with flexible substrates [5-8].

Thermoplastic polyurethane (TPU) is widely established as the matrix of choice for textile-integrated electronics due to its exceptional mechanical resilience and tunable elasticity, which closely mimic the modulus of conventional textiles [9, 10]. Unlike rigid polymers, TPU facilitates seamless integration through scalable processing techniques, including electrospinning, melt-lamination, and solution casting, ensuring robust interfacial adhesion with fibrous substrates. This structural compatibility minimizes delamination risks during cyclic deformation and washing, while its intrinsic chemical stability protects embedded active materials from environmental degradation [11-14].

Despite these mechanical advantages, the application of TPU in conventional capacitive sensing faces a fundamental performance ceiling. Significant sensitivity improvements (up to ~8.31 kPa^{-1}) in these systems are typically reliant on complex microstructuring of the dielectric layer [11, 15-24]. Without such intricate fabrication, standard dielectric films struggle to exceed Gauge Factors (GF) of ~1.05 [18, 19, 25]. This limitation necessitates a shift from bulk dielectric polarization to the high capacitance offered by Electrical Double Layer (EDL) mechanisms for more efficient signal transduction [26].

The incorporation of ionic Liquids (ILs) to form EDL interfaces has revolutionized this field by facilitating efficient charge separation at the nanometer scale [18, 22, 27, 28]. Among these, 1-butyl-3-methylimidazolium thiocyanate ([Bmim][SCN]) stands out for its high ionic conductivity, electrochemical stability, and compatibility with textile substrates [29, 30]. Recent works

View Article Online
DOI: 10.1039/D6TC00186F

demonstrate the potential of this approach. For instance, Keum et al. [31] achieved a sensitivity of 9.51 kPa^{-1} using a drop-molded 1-ethyl-3-methylimidazolium bis(trifluoromethylsulfonyl)imide [EMIM][TFSI] gel [31]. Similarly, Chen et al. [32] reported a wearable ionogel-based pressure sensor with a sensitivity of 33.8 kPa^{-1} enabled by a microstructured ionic interface, employing the IL 1-ethyl-3-methylimidazolium ethyl sulfate ([EMIM][ESO_4]) [32]. Additionally, Wang et al. [33] reported an iontronic wearable pressure sensor based on an IL gel electrolyte using ([EMIM][TFSI]), achieving a sensitivity of 106.01 kPa^{-1} and enabling detection of subtle physiological signals such as pulse and respiration [33].

Likewise, multimodal sensors combining silver nanowires with ionic gels have demonstrated GFs of ~2.74 [34]. In addition, Zhang et al. [35] reported a stretchable wearable strain sensor using an imidazolium-based IL ([EMIM][TFSI]), achieving a GF of 7.9 over a wide strain range (0.1–400%) [35]. More recently, MXene–ionogel composite strain sensors incorporating 1-butyl-3-methylimidazolium chloride ([BMIM]Cl) have been reported to achieve GFs of approximately 4.17 [36]. The obtained sensitivity values typically require specialized, lab-scale micro-fabrication steps that are incompatible with mass-production textile lines. This reliance on bespoke architectures limits the transition of iontronic sensors from academic prototypes to commercially viable products.

Thus, this work presents a material to architecture framework for multimodal iontronic textiles by incorporating different contents of the IL [Bmim][SCN] into both dense TPU matrices and porous neoprene-textile scaffolds. The influence of IL content (0, 20, 40 and 60% wt.) in the morphological, physical-chemical, electrical and mechanical properties of the composites was evaluated. The developed materials provided a path for the selective optimization of multimodal sensors in wearable electronics, by optimizing IL concentration to enhance ionic mobility and EDL area. Further, this work also allows to exploit the fabrication architecture with the use of dense and porous materials to facilitate pressure or strain sensing.

View Article Online
DOI: 10.1039/D6TC00186F

2. Experimental Section

2.1. Materials

Thermoplastic polyurethane (TPU), Texin® RxT70A, was purchased from ALBIS, Covestro Deutschland AG, with a molecular weight (Mw) of 80.000-120.000 g mol^{-1}. The ionic liquid (IL) 1-butyl-3-methylimidazolium thiocyanate ([Bmim] [SCN]) (>98% purity) was purchased from Ionic Liquids Technologies, IoLiTec, Germany. The neoprene textile (95% polyester and 5% spandex) was purchased from Almacenes Casa Ángel, Badajoz, Spain, and the stretchable conductive textile Shieldex® Technik-tex P180 + B from Shieldex (56% polyamide, 22% elastane, 26.5% Silver, 1.5% Silver Coating), Bremen, Germany. The solvent tetrahydrofuran (THF) (99.99% purity) was purchased from Fisher.

2.2. Fabrication of TPU/[Bmim][SCN] Films and Neoprene-Reinforced Scaffold

TPU and TPU/[Bmim][SCN] films were prepared by solvent casting (**Figure 1**). To obtain the TPU neat film, 1 g of polymer was dissolved in 15 mL of THF under magnetic stirring at 50 °C until completing dissolution. Then, the solution was placed in a Petri dish and the solvent was evaporated at room temperature for 24 hours.

For the preparation of TPU/[Bmim][SCN] films with 20, 40 and 60 % wt. IL content, a similar procedure was applied, with the previously dispersion of the IL in THF following by TPU addition.

Two distinct fabrication approaches were employed to prepare the textile/ TPU/[Bmim][SCN] composites. The first approach involved the lamination of previously prepared TPU and TPU/x[Bmim][SCN] films (where x represents the optimized concentration determined via film characterization) onto the conductive textile. To ensure adhesion, a precursor solution of the corresponding TPU/[Bmim][SCN] content was applied to the conductive textile via doctor-blade. The pre-cast film was immediately placed onto the wet coated conducting textile to minimize solvent evaporation. The assembly was subsequently cured in an oven (JP Selecta 2005165) at 50 ºC for 15 minutes to remove residual solvent and finalize the bond. This procedure was repeated for the reverse side to create a double-sided composite.

The second approach utilized a neoprene textile with 800 um thickness as a porous structural scaffold. The neoprene substrate was immersed in the respective TPU or TPU/[Bmim][SCN]

View Article Online
DOI: 10.1039/D6TC00186F

solutions at room temperature. Following immersion, the saturated neoprene was sandwiched between two layers of stretchable conductive textile with and sheet resistance of 2 Ω/□ and an average thickness of 0.57± 0.06 mm. Solvent evaporation was carried out under the same conditions (50 ºC for 15 minutes). Samples with an average thickness of 1 ± 0.1 mm and 1.5 ± 0.1mm and were obtained after direct bounding with IL /TPU and neoprene scaffold, respectively. The composites are designated by their matrix and IL content. Specifically, N-T_{neat} and T_{neat} represent the reference without IL content, for the porous neoprene-textile and dense TPU architectures, respectively, while N-T_{IL} and T_{IL} identify the optimized [Bmim][SCN] compositions with Shieldex textile electrodes.

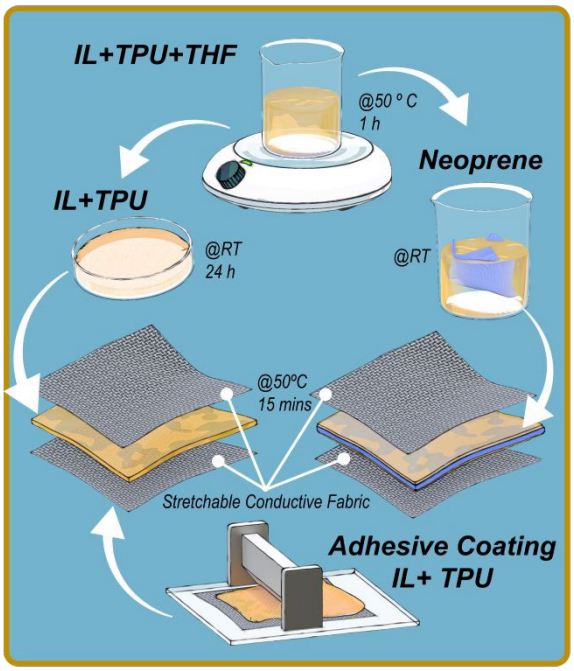

Figure 1 Experimental procedures used for the preparation of the TPU/[Bmim][SCN] films and the corresponding composite textile sensor.

2.3. Physicochemical and Electromechanical Characterization Methodologies

2.3.1. Morphology

The morphology of the samples with and without textile was assessed using a Scanning Electron Microscope (SEM) Carl Zeiss EVO-40, with an EDX (Oxford Instruments) detector to analyse IL

View Article Online
DOI: 10.1039/D6TC00186F

distribution by SEM-EDX measurements. Measurements were carried out at an accelerating voltage of 5 kV. Before the analysis, the samples were coated with gold (Au) by magnetron sputtering (Polaron SC502).

2.3.2. Physical-chemical characterization

Fourier transform infrared (FTIR) spectra were recorded in the attenuated total reflection (ATR) mode using a Perkin Elmer FTIR (Two) in the spectral range 4000 to 400 cm^{-1}, using 16 scans and a resolution of 4 cm^{-1}. Thermal evaluation was carried out by thermogravimetric analysis (TGA) and Differential scanning calorimetry (DSC). The TGA analysis was performed in an 851e Metter Toledo equipment between 25 and 650ºC, at 10 ºC/min under nitrogen atmosphere. DSC thermograms were recorded with a DSC822e (Mettler Toledo) between -40 and 270 ºC, at a heating rate of 10 ºC/min, under an atmosphere of high purity nitrogen at a constant flow of 20 mL/min.

2.3.3. Mechanical characterization

The mechanical properties were evaluated in the tensile mode at room temperature in a universal Linkam Scientific Instruments TST 350 testing machine (Temperature Controlled), comprising a Tensile Stress Testing Stage with a load cell of 200 N. The samples, with a rectangular shape (30 x 5 mm), were analysed in triplicate at a speed of 1 mm/min

2.3.4. Electrical and functional electromechanical characterization

Impedance spectroscopy (Z' and Z'') and capacity, were measured using an Impedance analyser (Palmsens4) with an amplitude voltage of 100mV at room temperature. Frequency sweeps were performed in the frequency range from 100 mHz to 1 MHz.

The dielectric constant (ε') was calculated using Eqs. (1):

$$\varepsilon' = \frac{C \cdot d}{\varepsilon_0 \cdot A} \quad (1)$$

where d is the thickness of samples, ε_0 is the permittivity of vacuum (8.85×10^{-12} $F \cdot m^{-1}$), and A is the electrode area. Electrodes with a diameter of 10 mm were places in a parallel plate configuration.

View Article Online
DOI: 10.1039/D6TC00186F

The ionic conductivity (σ) was calculated by using the equation (2)

$$\sigma = \frac{t}{A \times R_{ia}} \quad (2)$$

where t represents the thickness of the samples, A the surface area of electrodes, R_{ia} is the resistance determined by the intersection of the semicircle with the X-axis.

Pressure and tensile characterization were performed by measuring the capacitance as a function of deformation. The structures were attached to a universal testing machine (Shimadzu Autograph) platform with a load cell of 500 N at a stroke speed of 1mm/min. Tensile cycling and compression cycling loading was conducted for all samples up to a maximum deformation of 20% and 50 % of the sample thickness, respectively. Capacitance was measured using a LCR meter Hioki IM3536, with an amplitude voltage of 100 mV at 1 kHz, with ambient conditions (22ºC and relative humidity of 60%, approximately).

2.3.5. Ethics Information

All experimental protocols involving data acquisition of bending and pressure were performed as non-invasive self-experimentation by the first and corresponding author. Informed written consent was obtained prior to the collection of signals with a glove demonstrator. To ensure electrical and chemical safety, all measurements were conducted through the impermeable glove, which served as a dielectric barrier and prevent direct contact between the active composites and the skin.

3. Results and discussion

3.1. Physicochemical and Structural Analysis of TPU/IL Films

3.1.1. Morphology

The morphology of both neat TPU and TPU/[Bmim][SCN] films was evaluated by SEM. The cross-section images of the films are presented in **Figure 2**.

The cross-sectional SEM images of neat TPU films at room temperature reveal a compact morphology (**Figure 2a)**, consistent with previous reports in the literature [37]. With the incorporation of the different IL contents into the TPU matrix, noticeable changes occur into the

View Article Online
DOI: 10.1039/D6TC00186F

morphology of the films. **Figure 2a** show that, independently of the IL content, the inclusion of IL induces a porous morphology, where the degree of porosity of the films increases with the content of IL. Similar results were reported in [38], attributed to physical interactions between the polar solvent (THF) and the IL, as well as a phase separation occurring within the IL–solvent system [38]. As a result, during the solvent evaporation process, a phase separation of the IL-solvent mixture occurred, resulting in the encapsulation of the IL inside the pores after the solvent evaporated [38], due to the stronger interaction with the solvent than with the polymer matrix.

The homogeneity and dispersion of the IL into the TPU matrix was evaluated by SEM-EDX (**Figure 2a**) by the identification of the distribution of the S element of the IL. The S element of [Bmim][SCN] is present in the TPU/[Bmim][SCN] composites and well dispersed in the matrix. Further, the presence of the S element increases with the IL content in the composites from 20 to 60% wt.

At high concentration of IL, specifically for the TPU/60%[Bmim][SCN] sample, the IL cannot be contained fully within the matrix, and migrates to the surface over time (**Error! Reference source not found.**).

3.1.2. Physical-chemical characterization

The evaluation of the chemical characteristics of the materials was performed by FTIR-ATR measurements. As shown in **Figure 2b**, the chemical characteristics of TPU remain unchanged with the inclusion of [Bmim][SCN], being possible to observe the main absorption bands of the polymer.

The characteristic absorption bands of neat TPU are retained in the composites, confirming the preservation of the polymer structure. The absorption band at 3332 cm^{-1} corresponds to the N–H stretching vibration of the urethane group (–NHCOO–). Absorption bands at 2935 cm^{-1} and 2850 cm^{-1} are attributed to the asymmetric and symmetric stretching vibrations of $–CH_2$ groups, respectively. The carbonyl (C=O) stretching vibrations of amid group appear at 1730 cm^{-1} and 1700 cm^{-1}. The absorption band at 1533 cm^{-1} is related to the N–H bending vibration coupled with the C–N stretching, corresponding to the carbamate groups (–NHCOO–). Additionally, the bands

View Article Online
DOI: 10.1039/D6TC00186F

in the range of 1101–1108 cm^{-1} are associated with the ether group (C–O–C) [39, 40]. For the [Bmim][SCN] IL, specific bands are observed in the composites that are not present in the neat TPU spectrum. These include an absorption band at 2056 cm^{-1}, corresponding to the C≡N stretching vibration of the thiocyanate $[SCN]^-$ anion, and a band near 750 cm^{-1}, attributed to S–C stretching. The imidazolium cation exhibits characteristic C–H stretching bands at 3100 and 3145 cm^{-1}, and a C–N stretching band at 2056 cm^{-1} (possibly contributing to the increased intensity of this band). A broad absorption band near 3500 cm^{-1} is observed, corresponding to O–H stretching vibrations from adsorbed water, due to the hygroscopic nature of the IL [29, 30].

The influence of [Bmim][SCN] incorporation into the thermal properties of TPU was evaluated by DSC (**Figure 2c**). Neat TPU exhibits an endothermic peak at -2.4 °C, which corresponds to the glass transition temperature (Tg) of the polymer [41]. With the incorporation of [Bmim][SCN], an endothermic peak appears corresponding to the loss of water adsorbed by the compound [41, 42]. As the IL content increases from 20% to 60% wt., this band becomes more pronounced.

The thermal stability of the samples was evaluated by TGA measurements as shown in **Figure 2d**. Neat TPU presents a small initial mass loss around 100 °C, corresponding to the loss of water, followed by mass loss of 93.6% between 280 and 440 °C , corresponding to the main degradation of the polymer [43-45], attributed to the cleavage of urethane/urea bonds in the hard segments, followed by degradation of the soft segments (polyol)[43-46].

Upon IL incorporation into the TPU matrix, a decrease in the thermal stability is observed, being this decrease more noticeable for the composites with higher IL content. The samples incorporating 20 and 40% wt. present two degradation steps, the first ending around 100 °C and being attributed to moisture loss from the IL and the polymer matrix. The main degradation occurs in a single broad step, suggesting partial merging of hard and soft segment breakdown, likely caused by modifications in microphase separation induced by the IL. In contrast, the TPU/60%[Bmim][SCN] composite displays three distinct degradation stages: an initial low-temperature stage (~100 °C) associated with water loss, followed by two overlapping steps similar to neat TPU. This evolution of the degradation profile with increasing IL content reflects changes in polymer–ion interactions and segmental mobility that influence the thermal decomposition pathway [43-47].

View Article Online
DOI: 10.1039/D6TC00186F

The mechanical properties of the TPU/[Bmim][SCN] composite samples were analysed by tensile tests and the results are shown in **Figure 2e**. Stress vs strain curves reveal that neat TPU film presents a typical mechanical behavior of a thermoplastic polymer, characterized by a yielding region, separating the elastic from plastic region, being the behaviour consistent for all samples with the incorporation of [Bmim][SCN]

The Young's modulus (E), determined from the initial linear region of the stress–strain curves using the tangent method for a strain of 1%, progressively decreases with increasing IL concentration from 5.66 ± 0.10 MPa for neat TPU to 1.43 ± 0.05 MPa for TPU containing 60 wt% [Bmim][SCN]. This reduction in stiffness confirms that IL incorporation disrupts polymer–polymer interactions, enhances chain mobility, and thereby softens the TPU network [48, 49].

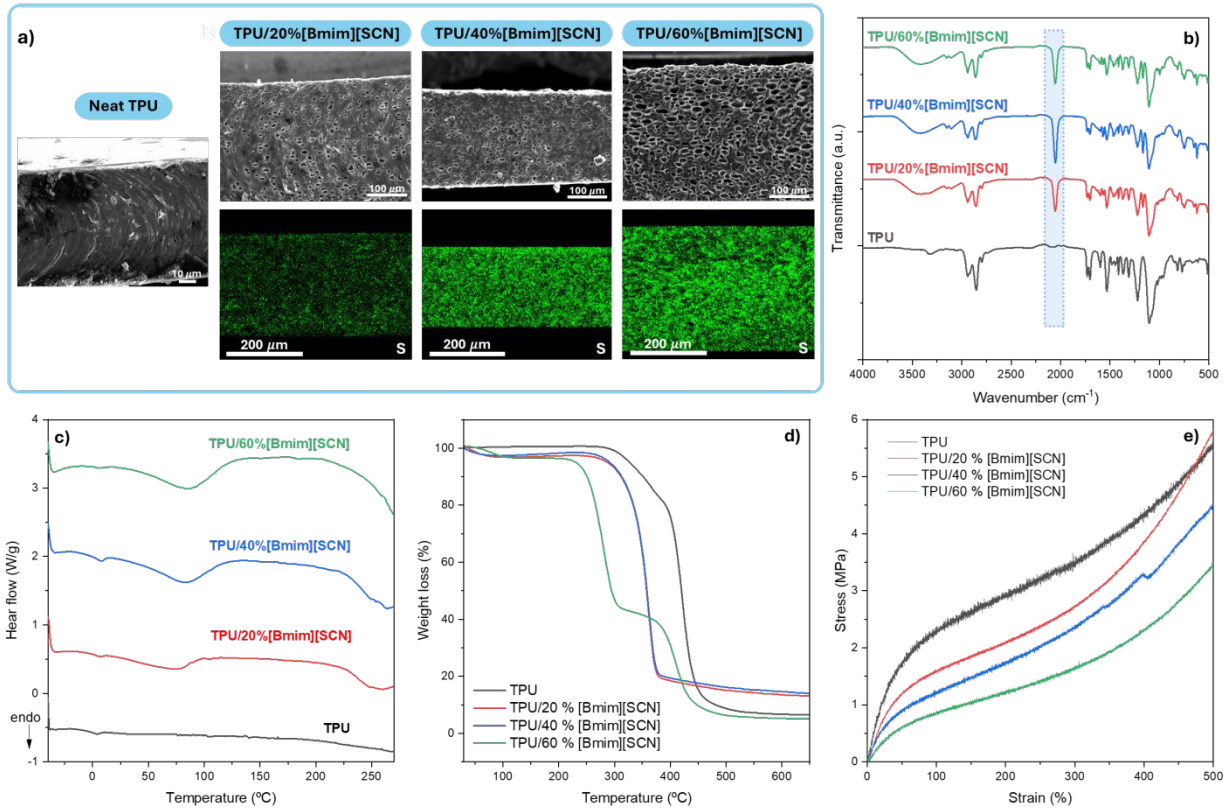

Figure 2. a) Cross-section SEM (top) and EDX (bottom) images of the TPU and TPU/[Bmim][SCN] films. b) ATR-FTIR spectra, c) DSC heating scans and d) TGA thermograms, e) Mechanical properties for neat TPU and TPU/[Bmim][SCN] composites with different contents of [Bmim][SCN].

View Article Online
DOI: 10.1039/D6TC00186F

3.1.3. Electrochemical Impedance Characterization

The electrical properties of neat TPU and TPU/[Bmim][SCN] films were evaluated, and the equivalent circuit and impedance results are presented in **Figure 3a-b**.

Neat TPU film exhibits a primarily resistive response with a slightly depressed semicircle, indicative of a distributed resistive-capacitive process. The incorporation of [Bmim][SCN] from 20 to 60 wt.%, monotonically reduces the Nyquist semicircle and shifts the high-frequency intercept (R_{ia}) to lower Z' values, consistent with increased ionic conductivity ($\sigma \propto 1/R_{ia}$). This behavior is more evident with higher IL concentrations. The increasing appearance of a low-frequency tail shows the distributed ion transport and diffusion, which are captured by a constant-phase element (CPE) in combination with diffusion (Warburg, W) term. The equivalent circuit comprising $R_b - R_{ia} - W$ in parallel with an interfacial capacitance CPE_{ia} (**Figure 3a**) replicates the transition from bulk to interface-dominated response.

The ionic conductivity (**Figure 3c**) increases with the increase of [Bmim][SCN] content. By using equation 2, ionic conductivities of 3.25±0.33 x 10^{-7} S/m, 3.45±0.45 x10^{-6} and 2.55±.25x10^{-5} S/m were obtained for 20%, 40% and 60% wt. of [Bmim][SCN] content in the TPU matrix, being consistent with the formation of continuous ion-transport within the TPU matrix.

Figure 3d presents the real permittivity (ε′) spectrum of the TPU/[Bmim][SCN] composite samples. Neat TPU exhibits a low and weakly dispersive ε′ behaviour across the measured frequency range, consistent with limited dipolar polarization and the absence of significant free charge carriers. With the incorporation of [Bmim][SCN], ionic charge carriers are introduced into the polymer matrix, being able to dynamically respond to the alternating electric field, particularly at low frequencies, where ions have sufficient time to migrate through the film matrix. These mobile ions accumulate at the electrode and interfacial boundaries, giving rise to electrode polarization [50]. As the [Bmim][SCN] content increases, the increase in ε′ is progressively more noticeable at higher frequencies. For all TPU/[Bmim][SCN] samples, ε′ increases significantly at low frequencies (<10 Hz), displaying the sample TPU/60 % [Bmim][SCN the highest $\varepsilon'$of 2203±50 at 1kHz (**Figure 3e**).

View Article Online
DOI: 10.1039/D6TC00186F

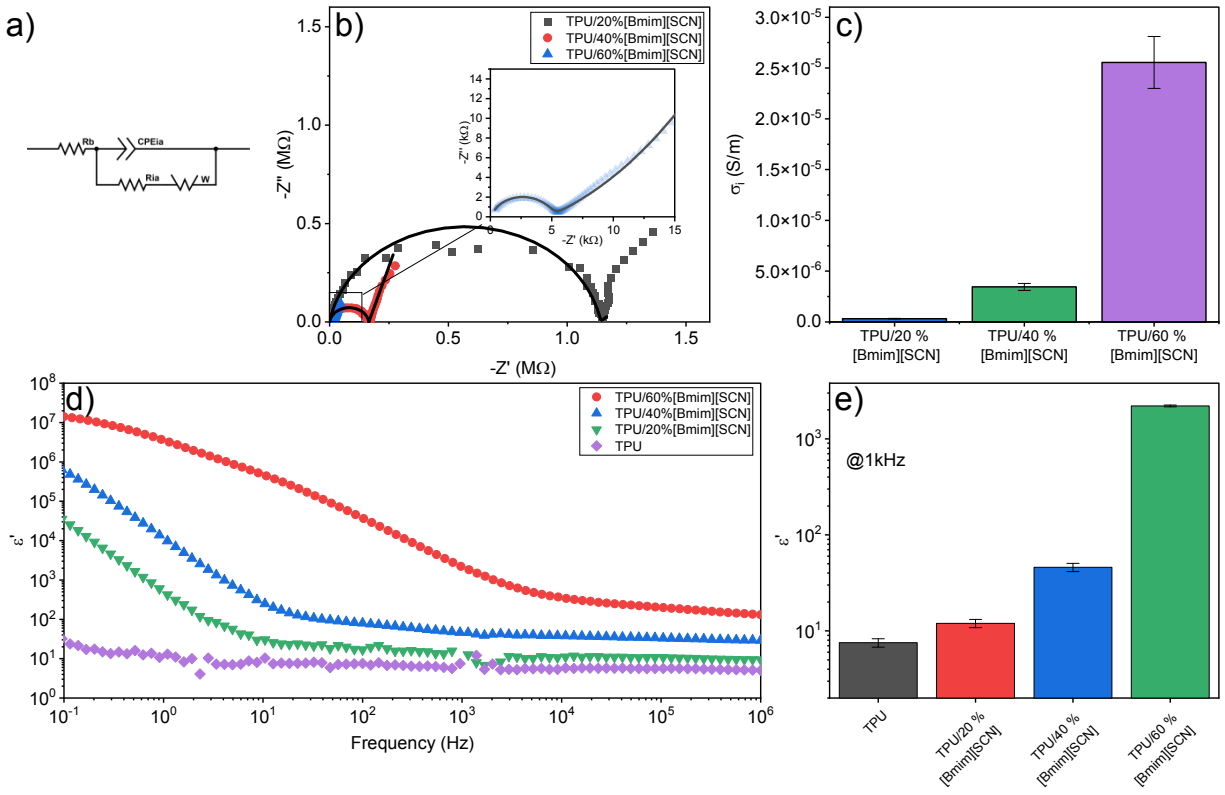

Figure 3 Impedance, transport, and dielectric proprieties of TPU and TPU/[Bmim][SCN] films. a) equivalent circuit, b) Nyquist impedance of solvent-cast TPU and TPU/[Bmim][SCN] at 20, 40, and 60 wt% (wt% relative to polymer+IL). The black solid line represents the fitting of the model shown within the figure. c) Conductivity extracted from high-frequency intercepts. d) Dielectric constant ε′ versus frequency, and e) Comparison of the dielectric constant for all samples at 1 kHz

Although the TPU/60% [Bmim][SCN] sample exhibited the highest permittivity and ionic conductivity, the IL could not be effectively retained within the polymer matrix, gradually migrating to the surface over time. This effect compromised the materials stability, making it unsuitable for further application. Therefore, the TPU/40% [Bmim][SCN] sample formulation was selected for subsequent incorporation into the textile porous structure, as it exhibited good surface stability with no visible IL segregation (**Figure S1**).

3.2. Integration of Neoprene Scaffold and Conductive Textile

Figure 4a-b compares the morphological behavior of the TPU/40%[Bmim][SCN] film sandwiched between two stretchable conductive textiles (T_{IL}) against the neoprene/ TPU/40%[Bmim][SCN] scaffold (N-T_{IL}), under both manual stretching and compression. It is also shown the mechanical compliance and structural retention of the composites.

View Article Online
DOI: 10.1039/D6TC00186F

Figure 4c shows cross-section SEM and SEM-EDX images of T_{neat}, T_{IL}, N-T_{neat} and N-T_{IL} samples. Film and neoprene scaffold reveal distinct fibrous and porous structures, exhibiting variations in internal architecture, fibre arrangement, and porosity.

SEM-EDX analysis was also performed on T_{IL} and N-T_{IL} with TPU/40%[Bmim][SCN] (**Figure 4c**), in order to identify the distribution of the IL though the S element of the IL. The S element from [Bmim][SCN] is present in the composites and is well dispersed within the matrix. Moreover, a more homogeneous distribution of the IL is observed in the N-T_{IL} composites, where the bulk T_{IL} appears more compact.

In addition, the chemical characteristics of neoprene, neoprene filled with TPU, and neoprene with TPU/40%[Bmim][SCN] were also evaluated. The characteristic absorption bands of neoprene are preserved in the composites, confirming the retention of its molecular structure. The peak at 1680 cm^{-1} is attributed to the C=C stretching vibration. The absorption bands at 966 cm^{-1} and in the 700–800 cm^{-1} range are associated with the out-of-plane C=C–H bending and the C–Cl stretching, respectively [51, 52]. Regarding the samples containing TPU and TPU/40% [Bmim][SCN], the main absorption bands of the thermoplastic polymer and the IL can also be observed.

The tensile properties of the neoprene scaffold, Shieldex conductive textile, and their respective multilayer composites(T_{neat}, T_{IL}, N-T_{neat} and N-T_{IL}) were evaluated (**Figure 4e)**. The stress–strain curves exhibit a characteristic bilinear behaviour, an initial low modulus region (0–100% strain) associated with the mechanical accommodation and reorientation of the textile fibres, followed by a linear elastic region where the fibres are under direct tension. Consequently, the Young's modulus (*E*) was calculated from the slope of the second linear region.

Neat neoprene exhibits a low Young modulus (1.6±0.2 MPa) and high elongation (above 500%) without total failure. Neat Shieldex textile presents a Young modulus of 3.2 ±0.1 MPa with a 300 % elongation at break, with individual yarn fibres initiating fracture at approximately 200% of elongation. The integration of TPU layer into neoprene leads to an increase in the Young modulus to 3.5± 0.3MPa, increasing tensile strength, and also to a elongation at break reduction to approximately 500%. The TPU matrix improves stress distribution across the fibre network, delaying individual yarn breakage until ~300% elongation.

View Article Online
DOI: 10.1039/D6TC00186F

The Shieldex/TPU/Shieldex structure (T_{neat}) presents a Young modulus of 3.3±0.5 MPa and elongation at break occurs at the same elongation that for the Shieldex textile alone (300%). For the Shieldex/TPU/IL/Shieldex (T_{IL}) system, [Bmim][SCN] IL incorporation induces a plasticization effect, reducing the Young modulus to 2.5±0.2 MPa and increasing the elongation to 310%.

The full Shieldex/Neoprene+TPU/Shieldex multilayer (N-T_{neat}) exhibits a significantly higher modulus (47 ± 1.2 MPa). This 15-fold increase implies a reinforcement effect, where TPU acts as an adhesive that impregnates the yarn fibres and constrains fibres intersections, preventing the sliding and forcing the fibres to undergo direct tension.

For the full Shieldex/Neoprene+TPU/IL/Shieldex multilayer (N-T_{IL}), the Young modulus reduces from 47 ± 1.2 MPa to 37.4 ± 1.4 MPa, due to the plasticization effect of the IL, similar to the T_{IL} sample. This reduction leads to the mechanical compliance of the composite, allowing for an increased elongation at break (450% to 500%) [49]. The fracture sequence of the multilayer system is characterized by the premature rupture of the conductive Shieldex layers at approximately 300% strain, followed by the total failure of the TPU and neoprene layers at around 500% for the N-T_{IL} sample.

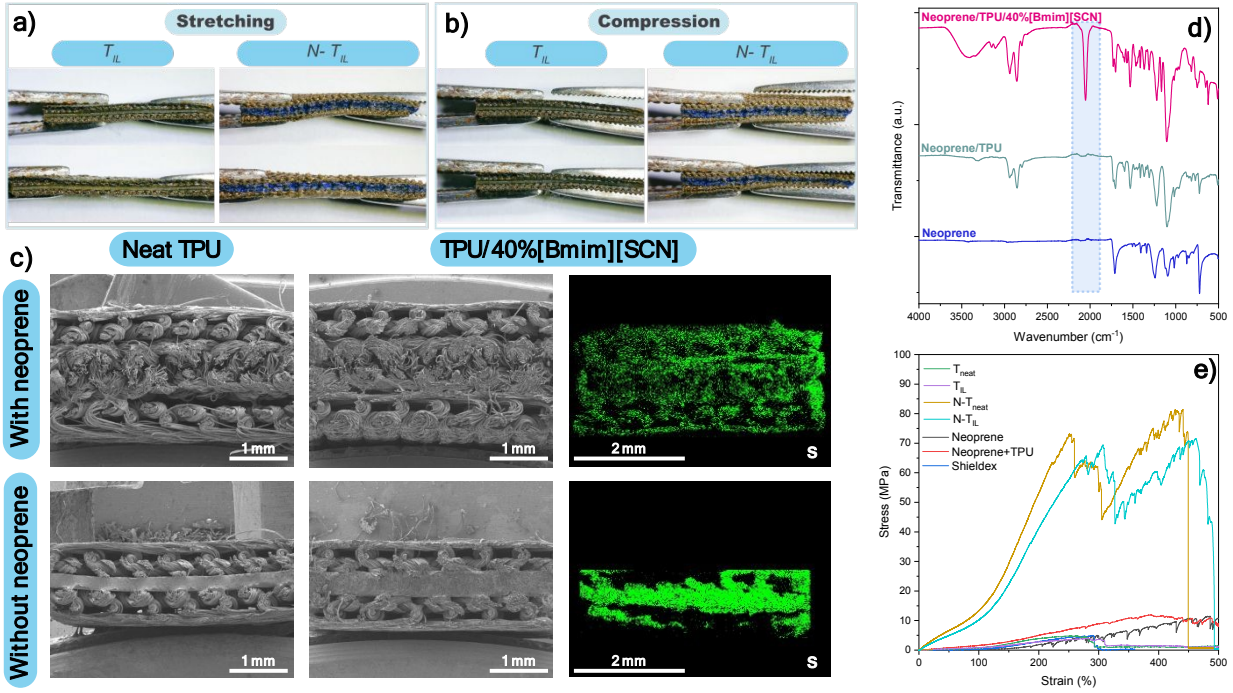

View Article Online
DOI: 10.1039/D6TC00186F

Figure 4 Cross-section SEM images of a TPU film placed between two stretchable conductive textiles, with and without an intermediate neoprene layer (T_{IL} vs. N-T_{IL}), q) under stretching and b) compression conditions. c) Cross-section SEM and SEM-EDX images of the neat TPU and TPU/40%[Bmim][SCN] films placed between two stretchable conductive textiles, with and without an intermediate neoprene layer. d) ATR-FTIR spectra. e) Mechanical properties of the textile composites.

3.3. Electrochemical Impedance Characterization

Impedance analysis reveals that the impregnation of neoprene with the TPU/IL mixture and lamination between stretchable conductors introduces a dominant interfacial contribution (**Figure 5a).** Compared to the films without the porous scaffold, the Nyquist spectrum displays two depressed semicircles, a high-frequency arc (R_{ia}) and an intermediate frequency arc (R_{ib}), followed by a low-frequency tail (W) (equivalent model in **Figure 5a**). We assign R_{ia} to fast response in the contact processes at the electrode–TPU/[Bmim][SCN], and R_{ib} to interfacial polarization across the porous neoprene-TPU/[Bmim][SCN] interface [53]. The subsequent low frequency tail is consistent with diffusion-limited transport and constant-phase behavior within the porous architecture.

The porous neoprene+TPU/40%[Bmim][SCN] sample exhibits a higher conductivity (8.8×10^{-6} S/m), attributed to the structural architecture of the neoprene scaffold, which provides interconnected macroscopic channels for ion migration. Unlike dense TPU matrix, where ion transport is constrained by the polymer chain dynamics of a homogeneous phase, the porous network facilitates a more direct transport pathway, reducing resistance and increasing the overall ion mobility[54, 55].

As shown in **Figure 5b**, the low-frequency response of the neoprene+TPU/40%[Bmim][SCN] sample is comparable to the high-loading of the TPU/60%[Bmim][SCN] film. This suggests that the available porous spaces into the porous scaffold improve the ions charge transport. Furthermore, the IL uptake by the textile fibers introduces Maxwell–Wagner–Sillars (MWS) interfaces [50], which amplify low-frequency interfacial polarization and contribute to the superior capacitive response of the composite system[56, 57].

View Article Online
DOI: 10.1039/D6TC00186F

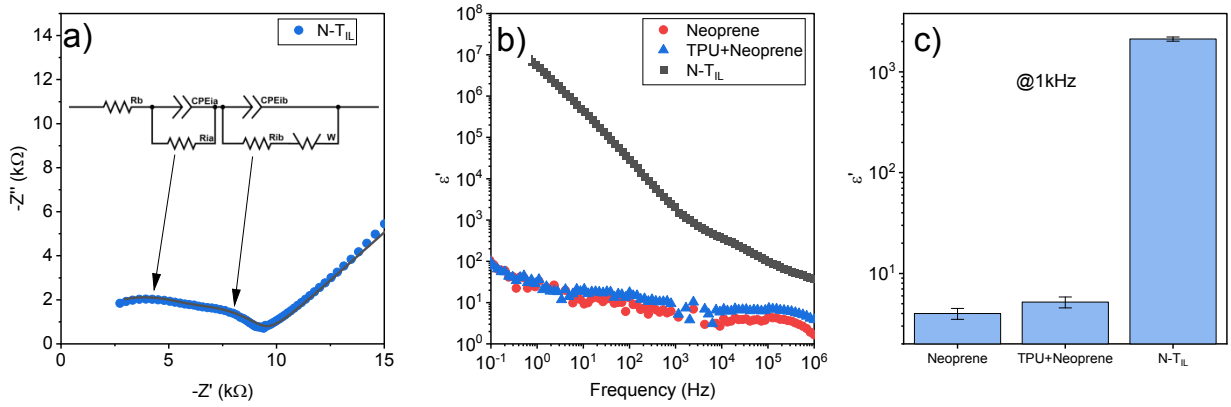

Figure 5 Impedance, and dielectric properties of the textile iontronic structure. a) Nyquist impedance of N-T$_{IL}$. The black solid line represents the fitting of the model shown in the figure. b) Dielectric constant ε′ versus frequency, and c) Comparison of the dielectric constant for textile samples at 1 kHz

3.4. Sensing performance to stretching and pressure

3.4.1. Stretching sensing behavior

Upon the application of a tensile strain, the T_{neat} and T_{IL} films exhibit a significant reduction of the film thickness and an alteration of the contact geometry at the electrode interfaces, increasing the samples capacitance(**Figure 6a)**. Simultaneously, the [Bmim][SCN] ions redistribute within the polymer matrix, building and depleting the EDL [58, 59].

Figure 6b and 6c show the films properties under cyclic stretching. T_{neat} exhibits a highly repeatable capacitance variation $\Delta C/C_0$that tracks without deviation with the tensile change $\Delta\varepsilon/\varepsilon_0$ (where Δε represents the strain variation and ε_0 the initial length). The T_{IL} displays a higher$\Delta C/C_0 = 0.3$ for a $\Delta\varepsilon/\varepsilon_0 = 0.5$ compared with the T_{neat} with a $\Delta C/C_0 = 0.06$ for the same tensile change without apparent drift. **Figure 6d** shows the calculated sensitivity ($\Delta C/C_0/\Delta\varepsilon/\varepsilon_0$) for T_{neat} and T_{IL}. T_{neat} shows $S = 0.13$, with hysteresis of 13.6% while T_{IL} reaches $S = 0.58$, with a hysteresis of 6.9%. Thus, the results revealed that the presence of IL and IL content increase strengthens strain-to-capacitance transduction.

Figure 6f-h show the porous samples response under cyclic stretching and the calculated sensitivity. N-T_{neat} slightly increases $\Delta C/C_0$relative to T_{neat} (0.13 to 0.19) maintaining repeatability, with a slight increase in hysteresis to 8.8%. N-T_{IL}, shows a noisy $\Delta C/C_0$ with very low repeatability. Contrary to dense films (T_{IL}), where stretching modulated thickness leads to a higher EDL polarization and high capacitance variation, in the porous architecture, tensile strain

View Article Online
DOI: 10.1039/D6TC00186F

hinders the contact networks (breaking the ionic path) (**Error! Reference source not found.**) and introduces ionic/capacitive heterogeneity, suppressing sensitivity and stability (**Figure 6e)** [60]. Thus, based on these results, the T_{IL} film is the most effective for strain sensing. The dynamic response of the T_{IL} strain sensor was characterized using a manual strain to evaluate the time resolution (**Figure S3).** The sensor exhibited a response time of 180 ms and a recovery time of 250 ms. Although the stimulus was applied manually, the signal stabilization occurred in a short time with a clear return to the baseline.

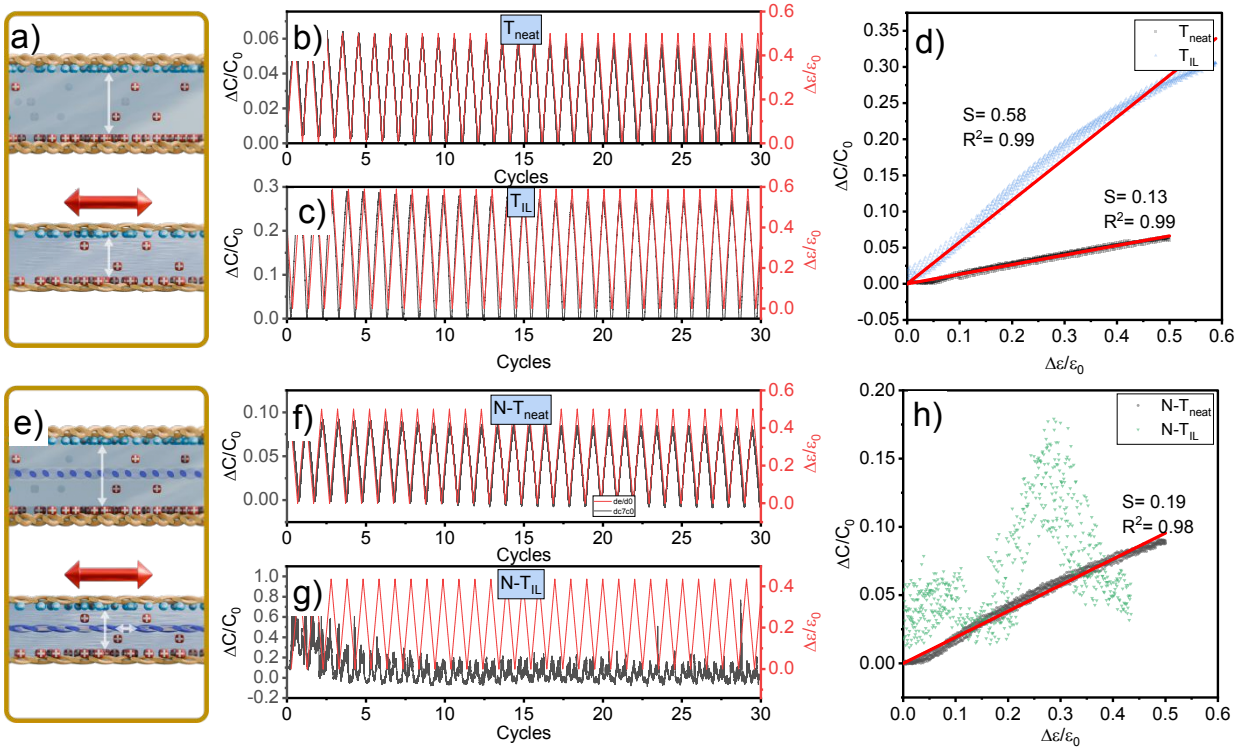

Figure 6. Strain-iontronic transduction under tensile loading. a) Schematic of ion redistribution and EDL effects in T_{IL} sample during stretching. Cyclic uniaxial stretching of dense films: normalized capacitance change $\Delta C/C_0$(black) and normalized tensile change $\Delta\varepsilon/\varepsilon_0$(red) for b) T_{neat} and c) T_{IL}. d) Sensitivity extracted as the slope S of $\Delta C/C_0$ versus $\Delta\varepsilon/\varepsilon_0$ .e) Schematic of EDL modulation in the porous structure under stretching. Cyclic stretching of porous devices: f) N-T_{neat} and g) N-T_{IL}; $\Delta C/C_0$(black) and $\Delta\varepsilon/\varepsilon_0$(red) plotted as in b–c. h) Corresponding sensitivity.

3.4.2. Pressure sensitivity

The proposed sensing mechanisms, illustrated in **Figure 7a and 7e,** show the mechanism and response under compression. Under an applied AC field, mobile [Bmim][SCN] ions migrate within the TPU matrix and accumulate at the electrode–polymer interfaces, forming EDL. When a compressive load is applied, the film thickness decreases, reducing the distance between the

View Article Online
DOI: 10.1039/D6TC00186F

electrodes and at the same time reducing the ion transport path and facilitating higher charge accumulation at the interfaces resulting in a capacitance increase.

Cyclic compression is displayed **Figure 7b and c**. T_{neat} shows a small, repeatable $\Delta C/C_0$with minor drift over 500 cycles (5 hours) For the T_{IL} sample it shows significantly higher capacitance gain per kPa. **Figure 7d** show the pressure sensitivity for the films, displaying a linear fit, the results are $S = 2.78 \times 10^{-4}$ kPa^{-1}for T_{neat} and $S = 8.78 \times 10^{-4}$ kPa^{-1}for T_{IL}. Showing that in this geometry, IL addition slightly increases compression sensitivity despite enhancing dielectric polarization, mostly because of the low compression ability of the TPU composite. The T_{neat} sample shows a hysteresis of 11.8 % for all measured range, the sample with the 40 wt.% IL addition shows a hysteresis of around 8.4%, primarily above 30 kPa.

In the T_{IL} with neoprene structure (**Figure 7e)**, compression not only reduces film thickness but also reduces the interfacial resistance in the textile–polymer interfaces. The porous neoprene structure deforms elastically, accommodating local strain without disrupting ionic continuity, leading to higher charge accumulation at the electrode–polymer boundaries[61, 62].

The introduction of the neoprene scaffold (N-T_{neat}) (**Figure 7f)** lead to an undesirable increase in drift with the progression of the compression cycles. Compression cycles for the N-T_{IL} (**Figure 7g**) display lower cumulative drift when compared with N-T_{neat} sample.

For the porous structure, the sensitivity increases with the incorporation of IL as shown in **Figure 7h**. The fitted slope for N-T_{neat} shows a sensitivity $S \approx 6.5 \times 10^{-4}$ kPa^{-1}, while for the N-T_{IL} sample, the sensitivity increases to $S \approx 1.8 \times 10^{-2}$ kPa^{-1} for the pressure range of 0 to 20 kPa. A secondary fit at higher loads (above 20 kPa) gives a sensitivity of $S \approx 3 \times 10^{-3}$ kPa^{-1}, indicating an onset of structural saturation within the neoprene structure. Above 80 kPa the curve saturates. limiting the material response for pressures below 80 kPa. The N-T_{IL} sample shows approximately 6× more sensitivity than N-T_{neat} and ~20× more sensitivity than the T_{neat} sample. Similarly to the samples without the neoprene textile, the hysteresis also decreases slightly, from 16.6 % to 14.7% for the N-T_{neat} and N-T_{IL}, respectively.

View Article Online
DOI: 10.1039/D6TC00186F

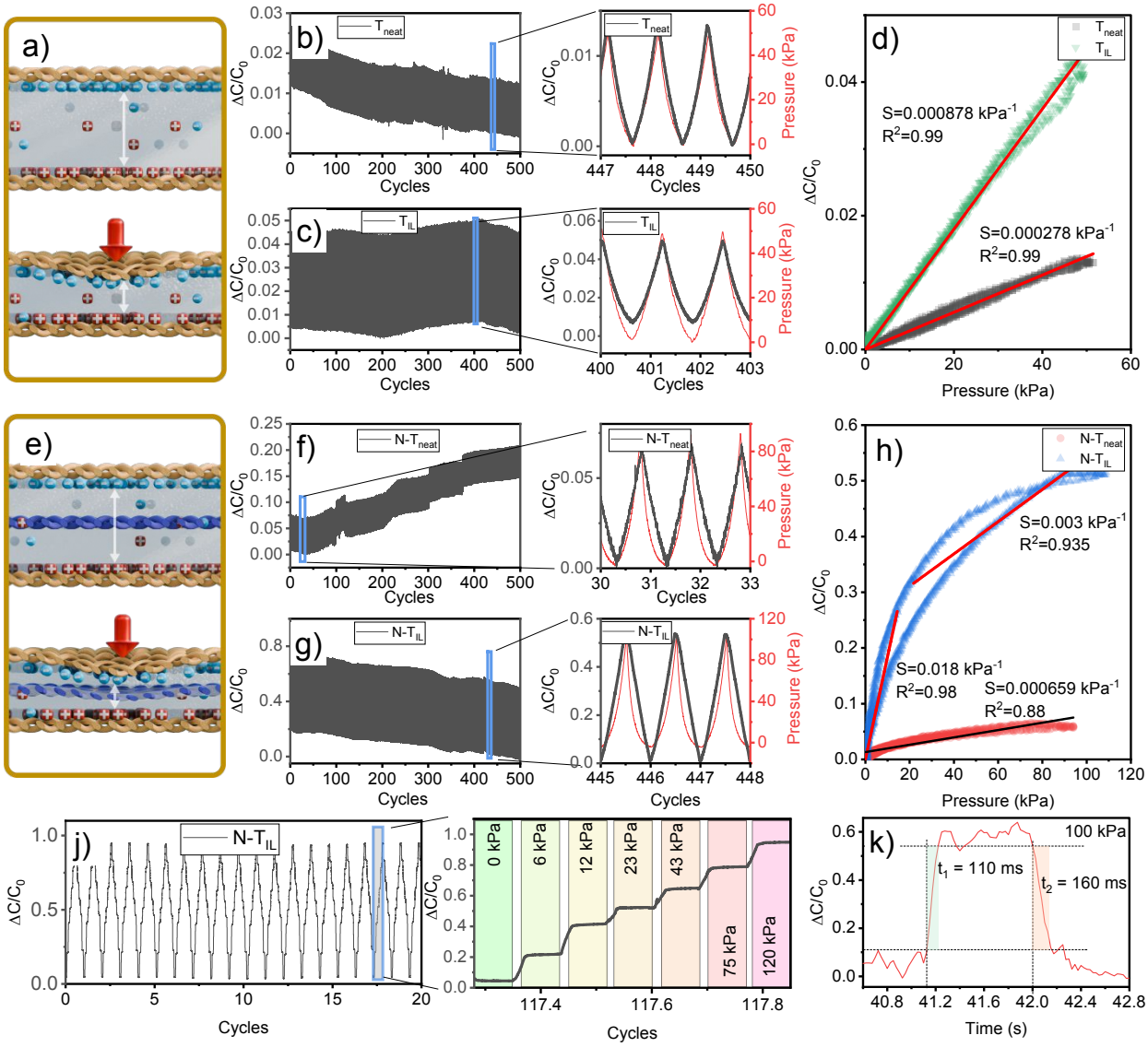

Figure 7 a) Schematic representation of ion redistribution and EDL modulation in TPU/[Bmim][SCN] during compression. b–c) Cyclic compression for T_{neat} and T_{IL} (capacitance variation $\Delta C/C_0$ in black, with pressure trace in red). d) Film sensitivities from linear fits of $\Delta C/C_0$ vs pressure e) Schematic of ion redistribution and EDL modulation in N-T_{IL} during compression. Cyclic compression for porous structure f) N-T_{neat} and g) N-T_{IL}. h) Pressure sensitivity for porous structures. j) Step-and-hold tests with pressure steps from 0 to 120 kPa with 10 s holds. k) Response (t_1) and recovery (t_2) times for a 100 kPa compression step for the N-T_{IL} sample.

Based on the higher sensitivity results obtained for the N-T_{IL} sample the stability and resolution was evaluated in incremental step-loading (**Figure 7j**), The sample exhibits a repeatable increments in $\Delta C/C_0$ proportional to the applied pressure steps , with each 10 seconds holds, demonstrating negligible signal drift (relative fluctuation < 4%). While the response remains stable across the full range (0-120 kPa), a progressive attenuation in the signal increment is observed at

View Article Online
DOI: 10.1039/D6TC00186F

higher pressures, correlating with the nonlinear behavior presented in the sensitivity fitting originating from the compressive saturation of the porous neoprene scaffold as it reaches its densification limit.

The dynamic characteristics were quantified under a 100 kPa pressure pulse (**Figure 7k)**. The N-T_{IL} sample achieved a response time ($t_{90\%}$) of 110 ms and a recovery time ($t_{10\%}$) of 160 ms.

3.5. Proof of concept: Glove-Integrated Gesture and Force Recognition

As proof of concept to validate the integration in a wearable application, the T_{IL} sample was attached to a glove across a finger joint and the response was evaluated under bending. In the same finger a N-T_{IL} sample was placed at the fingertip and the response was evaluated under compression(**Figure 8**). These samples were selected based on T_{IL} higher performance in tensile deformation results and the N-T_{IL} higher performance in the compression tests.

The sensors were connected to the digital pins of a microcontroller (ESP32 development board) via an operational amplifier-based relaxation oscillator circuit. This configuration modulates a continuous square waveform output, where the oscillation frequency varies as function of the capacity change of the sensors [63]. The microcontroller uses the internal timer to quantify the pulse density within a 100 ms window, giving a digital output in counts.

During repetitive flex-extend motion (**Figure 8a**), the sensor follows the bending of the finger with high amplitudes, minimal baseline drift, and high reproducibility. Dwelling plateaus at the middle and end bending radius range show a stable signal with negligible drift over the observation window.

View Article Online
DOI: 10.1039/D6TC00186F

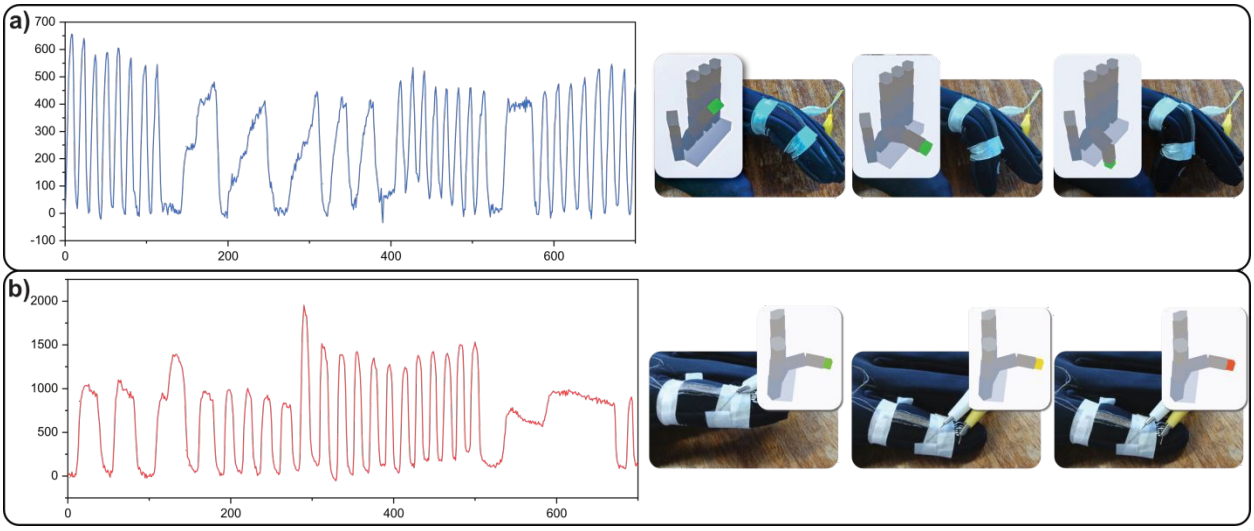

Figure 8. Wearable proof-of-concept system consisting in the iontronic sensors mounted in a glove. a) Signal from repetitive bending of the T_{IL} sensor and video frames showing finger joint flexion. b) Signal from fingertip pressing with the N-T_{IL} sensor and frames illustrating localized fingertip pressure.

Under localized pressure in the fingertip(**Figure 8b**) the N-T_{IL}, signal increases with the applied force as the finger is pressed on the table, dwelling plateaus at in the middle and end regions also show the ability to detect different detection levels. The sensor signal was feed to interface representing a 3D and with a fingertip, showing the pressure as a color variation (green to red gradient). The frames in confirm that these values coincide with contact growth with the table at the fingertip (**video S1 of support information**).

To assess the environmental robustness against humidity environments, required for some wearable applications, long-term and humidity-dependent stability tests were performed for N-T_{IL} and T_{IL} samples(**Figure S4**). Under a constant compressive load of 100 kPa (60% RH) for 12 h, the N-T_{IL} sensor exhibited a baseline drift of 3.5%. However, the sample shows significant sensitivity to ambient moisture during humidity cycling (40% to 90% RH). Further, the sample exhibited a relative capacitance variation to humidity $\Delta C/C_0$ of 0.1, with a noticeable drift of approximately 83%. This behavior is attributed to the hygroscopic behavior of the IL[64] and the moisture adsorption within the neoprene scaffold.

The dense T_{IL} sample demonstrated over a 12 h period a baseline drift within 9.3%. During humidity cycling, the T_{IL} sample shows an increase in $\Delta C/C_0$ of 0.3 with significantly lower drift of 6.9% (the dense TPU matrix limits the IL exposure to ambient moisture compared with porous neoprene scaffold). To mitigate environmental sensibility in practical wearable contexts,

View Article Online
DOI: 10.1039/D6TC00186F

additional hydrophobic encapsulation will be required, such as a thin over-molded TPU protective layer, to ensure reliability in sweat prone or high humidity environments.

4. Conclusions

This work demonstrates the successful development of hybrid TPU/[Bmim][SCN] iontronic materials and textile-based sensors for wearable force and deformation sensor applications.

The incorporation of [Bmim][SCN] (20, 40 and 60 wt.%) into a TPU matrix induces a porous morphology in films whose degree of porosity increases with IL content, without modifying the physical-chemical properties and thermal behaviour of the TPU matrix. Between all the IL contents, the IL concentration of 40 wt.% revealed the optimal threshold for maximizing ionic conductivity while ensuring long-term structural stability and preventing surface IL release.

Regarding sensing performance, it was achieved by the interplay between material density and architectural porosity. Under tensile strain, dense T_{IL} films provide a linear response (S = 0.58). Conversely, the integration of a porous neoprene scaffold enables a six times increase in pressure sensitivity (1.8×10^{-2} kPa^{-1}).

The successful integration of these sensors in a glove-mounted prototype demonstrated accurate detection of bending and pressing signals, confirming the practical utility of these multifunctional materials in wearable electronics.

Although neoprene scaffolds exhibited promising advantages in pressure sensing, environmental tests revealed a sensitivity to humidity in porous structures. Thus, whenever needed, environmental interference can be reduced though the application of a dense TPU encapsulation layer.

ACKNOWLEDGMENTS

This work was supported by the Portuguese Foundation for Science and Technology (FCT) in the framework of the Strategic Funding UID/00686/2025: Chemistry Centre of the University of Minho (CQ-UM) (DOI: https://doi.org/10.54499/UID/00686/2025) and UID/04650/2025: Physics Centre of Minho and Porto Universities (CF-UM-UP) (DOI: https://doi.org/10.54499/UID/04650/2025).D.M.C. also thank the FCT for financial support in the framework of the contract 10.54499/2020.02915.CEECIND/CP1600/CT0029,

View Article Online
DOI: 10.1039/D6TC00186F

10.54499/2022.03931.PTDC funded by national funds through FCT and by the ERDF through the COMPETE2020 Programa Operacional Competitividade e Internacionalização (POCI) and also COMPETE2030-FEDER-00760700, nº16437. This study forms part of the Advanced Materials program and was supported by MCIN with funding from European Union NextGenerationEU (PRTR-C17.I1) and by the Basque Government under the IKUR program and Grupos Consolidados (IT1756-22). Funding from the Basque Government Industry Department under the ELKARTEK program is also acknowledged. Technical and human support provided by SGIker (UPV/EHU, MICINN, GV/EJ, EGEF, and ESF) is gratefully acknowledged.

5. References

1. Aroganam, G., N. Manivannan, and D.J.S. Harrison, *Review on wearable technology sensors used in consumer sport applications.* 2019. **19**(9): p. 1983.
2. Burmaoglu, S., et al., *Evolution map of wearable technology patents for healthcare field.* 2018: p. 275-290.
3. Godfrey, A., et al., *From A to Z: Wearable technology explained.* 2018. **113**: p. 40-47.
4. Thakkar, H.K., et al., *Applications of wearable technologies in healthcare: An analytical study*, in *5G IoT and Edge Computing for Smart Healthcare*. 2022, Elsevier. p. 279-299.
5. Chen, G., et al., *Electronic textiles for wearable point-of-care systems.* 2021. **122**(3): p. 3259-3291.
6. Galli, V., et al., *Passive and Wireless All-Textile Wearable Sensor System.* 2023. **10**(22): p. 2206665.
7. Islam, G.N., A. Ali, and S.J.C. Collie, *Textile sensors for wearable applications: A comprehensive review.* 2020. **27**: p. 6103-6131.
8. Yin, J., et al., *Flexible textile-based sweat sensors for wearable applications.* 2023. **13**(1): p. 127.
9. Chatterjee, K. and T.K. Ghosh, *3D Printing of Textiles: Potential Roadmap to Printing with Fibers.* Advanced Materials, 2020. **32**(4): p. 1902086.
10. Happonen, T. and M. Paakkolanvaara. *Stretching Reliability of SMD Electronics Integrated on Elastic Fabric*. in *2024 International Conference on the Challenges, Opportunities, Innovations and Applications in Electronic Textiles (E-Textiles)*. 2024.
11. Wang, J., et al., *Highly sensitive, breathable, and flexible pressure sensor based on electrospun membrane with assistance of AgNW/TPU as composite dielectric layer.* 2020. **20**(9): p. 2459.
12. Zhou, Y. and R.J.P.f.A.T. Stewart, *Highly flexible, durable, UV resistant, and electrically conductive graphene based TPU/textile composite sensor.* 2022. **33**(12): p. 4250-4264.
13. Zhou, Z., et al., *Flexible strain sensors based on thermoplastic polyurethane fabricated by electrospinning: A review.* 2024. **24**(15): p. 4793.
14. Jin, X., et al., *A highly sensitive and wide-range pressure sensor based on orientated and strengthened TPU nanofiber membranes fabricated by a conjugated electrospinning technology.* 2023. **14**: p. 100491.

View Article Online
DOI: 10.1039/D6TC00186F

15. Chen, Y., et al., *A highly sensitive and wearable pressure sensor based on conductive polyacrylonitrile nanofibrous membrane via electroless silver plating.* 2020. **394**: p. 124960.
16. Keum, K., et al., *Fully-integrated wearable pressure sensor array enabled by highly sensitive textile-based capacitive ionotronic devices.* 2021. **79**: p. 105479.
17. Ko, Y., C.C. Vu, and J.J.S. Kim, *Carbonized cotton fabric-based flexible capacitive pressure sensor using a porous dielectric layer with tilted air gaps.* 2021. **21**(11): p. 3895.
18. Liu, J., et al., *Stretchable and High-Performance Fibrous Sensors Based on Ionic Capacitive Sensing for Wearable Healthcare Monitoring.* 2025. **12**(1): p. 2412859.
19. Yang, W., et al., *A breathable and screen-printed pressure sensor based on nanofiber membranes for electronic skins.* 2018. **3**(2): p. 1700241.
20. Yu, P., et al., *All-fabric ultrathin capacitive sensor with high pressure sensitivity and broad detection range for electronic skin.* 2021. **13**(20): p. 24062-24069.
21. Zhang, Q., et al., *Textile-only capacitive sensors for facile fabric integration without compromise of wearability.* 2019. **4**(10): p. 1900485.
22. Su, M., et al., *Textile-based flexible capacitive pressure sensors: A review.* 2022. **12**(9): p. 1495.
23. Huang, Y., et al., *Emerging technologies of flexible pressure sensors: materials, modeling, devices, and manufacturing.* 2019. **29**(12): p. 1808509.
24. Sonil, N.I., et al., *Wearable strain sensors for human motion detection and health monitoring based on hybrid graphite-textile flexible electrodes.* 2023. **26**: p. 764-774.
25. Atalay, O.J.M., *Textile-based, interdigital, capacitive, soft-strain sensor for wearable applications.* 2018. **11**(5): p. 768.
26. Wu, J., *Understanding the Electric Double-Layer Structure, Capacitance, and Charging Dynamics.* Chemical Reviews, 2022. **122**(12): p. 10821-10859.
27. Wang, Y. *Research on Flexible Capacitive Sensors for Smart Textiles*. in *Journal of Physics: Conference Series*. 2022. IOP Publishing.
28. Zhou, Z., et al., *Textile-based mechanical sensors: A review.* 2021. **14**(20): p. 6073.
29. Cabeza, O., et al., *Synthesis, microstructure and volumetry of novel metal thiocyanate ionic liquids with [BMIM] cation.* 2019. **283**: p. 638-651.
30. Serra, J., et al., *Ionic liquid based Fluoropolymer solid electrolytes for Lithium-ion batteries.* 2020. **25**: p. e00176.
31. Keum, K., et al., *Highly sensitive textile-based capacitive pressure sensors using PVDF-HFP/ionic liquid composite films.* 2021. **21**(2): p. 442.
32. Chen, Z.-J., et al., *An ultra-tough and ultra-sensitive ionogel pressure/temperature sensor enabled by hierarchical design of both materials and devices.* 2023. **11**(15): p. 8359-8367.
33. Wang, J., et al., *Flexible iontronic sensors with high-precision and high-sensitivity detection for pressure and temperature.* 2023. **39**: p. 101544.
34. Keum, K., et al., *Mechanically robust textile-based strain and pressure multimodal sensors using metal nanowire/polymer conducting fibers.* 2022. **25**(4).
35. Zhang, S.-H., et al., *Wearable wide-range strain sensors based on ionic liquids and monitoring of human activities.* 2017. **17**(11): p. 2621.
36. Wan, Y., et al., *High-performance and frost-resistance MXene co-ionic liquid conductive hydrogel printed by electrohydrodynamic for flexible strain sensor.* 2024. **669**: p. 688-698.
37. Wu, T. and B.J.S.R. Chen, *Facile fabrication of porous conductive thermoplastic polyurethane nanocomposite films via solution casting.* 2017. **7**(1): p. 17470.

View Article Online
DOI: 10.1039/D6TC00186F

38. Fernandes, L.C., et al., *Ionic-liquid-based printable materials for thermochromic and thermoresistive applications.* 2019. **11**(22): p. 20316-20324.
39. Mi, H.-Y., et al., *Characterization of thermoplastic polyurethane/polylactic acid (TPU/PLA) tissue engineering scaffolds fabricated by microcellular injection molding.* 2013. **33**(8): p. 4767-4776.
40. Wang, M., et al., *Research on the performance and mechanism of asphalt modified by thermoplastic polyurethane with different chemical structures.* 2023. **409**: p. 133814.
41. Hossieny, N., et al., *Characterization of hard-segment crystalline phase of thermoplastic polyurethane in the presence of butane and glycerol monosterate and its impact on mechanical property and microcellular morphology.* 2017. **112**: p. 208-218.
42. Pushparaj Subramaniyan, S., et al., *Moisture-Driven Morphology Changes in the Thermal and Dielectric Properties of TPU-Based Syntactic Foams.* 2025. **17**(5): p. 691.
43. Zhao, W., et al., *A Comprehensive study on the degradation behavior and mechanism of expanded thermoplastic polyurethane.* 2025. **17**(8): p. 1033.
44. Godlewska, J., J. Smorawska, and E.J.M. Głowińska, *Chemical Structure and Thermal Properties versus Accelerated Aging of Bio-Based Poly (ether-urethanes) with Modified Hard Segments.* 2024. **29**(15): p. 3585.
45. Dorigato, A., D. Rigotti, and A.J.F.i.M. Pegoretti, *Thermoplastic polyurethane blends with thermal energy storage/release capability.* 2018. **5**: p. 58.
46. Duval, A. and L.J.P.C. Avérous, *From thermoplastic polyurethane to covalent adaptable network via reversible photo-crosslinking of a biobased chain extender synthesized from caffeic acid.* 2023. **14**(22): p. 2685-2696.
47. Belesov, A.V., et al., *New insights into the thermal stability of 1-butyl-3-methylimidazolium-based ionic liquids.* 2022. **23**(18): p. 10966.
48. Eom, Y., et al., *Mechano-responsive hydrogen-bonding array of thermoplastic polyurethane elastomer captures both strength and self-healing.* 2021. **12**(1): p. 621.
49. Fernandes, L.C., et al., *Ionic-triggered magnetoelectric coupling for magnetic sensing applications.* 2022. **29**: p. 101590.
50. Thoms, E., et al., *Dielectric study on mixtures of ionic liquids.* Scientific Reports, 2017. **7**(1): p. 7463.
51. Bouaziz, R., et al., *Elastic properties of polychloroprene rubbers in tension and compression during ageing.* 2020. **12**(10): p. 2354.
52. Ismail, A.S. and E.A.J.P.i.P.S. Ismail, *Preparation and Characterization Challenges in Hydroxylation of Neoprene Rubber.* 2018. **2**(1): p. 1-4.
53. Isaac, J.A., et al., *Electrochemical Impedance Spectroscopy of PEO-LATP Model Multilayers: Ionic Charge Transport and Transfer.* ACS Applied Materials & Interfaces, 2022. **14**(11): p. 13158-13168.
54. Zhang, J., et al., *Honeycomb-like porous gel polymer electrolyte membrane for lithium ion batteries with enhanced safety.* Scientific Reports, 2014. **4**(1): p. 6007.
55. Permatasari, A., et al., *Porosity and tortuosity dynamics and their impact on lithium-ion battery performance with different separator structures.* Journal of Power Sources, 2025. **647**: p. 237278.
56. Islam, M.R., et al., *Smart Electronic Textile-Based Wearable Supercapacitors.* Advanced Science, 2022. **9**(31): p. 2203856.

View Article Online
DOI: 10.1039/D6TC00186F

57. Durak, O., et al., *Composites of porous materials with ionic liquids: Synthesis, characterization, applications, and beyond.* Microporous and Mesoporous Materials, 2022. **332**: p. 111703.
58. Pullanchiyodan, A., et al., *MnOx-Electrodeposited Fabric-Based Stretchable Supercapacitors with Intrinsic Strain Sensing.* ACS Applied Materials & Interfaces, 2021. **13**(40): p. 47581-47592.
59. Han, J., et al., *Hierarchically Porous Wearable Composites for High-Performance Stretchable Supercapacitors.* Advanced Science, 2025. **12**(25): p. 2500835.
60. Liu, Z., et al., *Functionalized Fiber-Based Strain Sensors: Pathway to Next-Generation Wearable Electronics.* Nano-Micro Letters, 2022. **14**(1): p. 61.
61. Siretanu, I., et al., *Direct observation of ionic structure at solid-liquid interfaces: a deep look into the Stern Layer.* Scientific Reports, 2014. **4**(1): p. 4956.
62. Bazant, M.Z., B.D. Storey, and A.A. Kornyshev, *Double Layer in Ionic Liquids: Overscreening versus Crowding.* Physical Review Letters, 2011. **106**(4): p. 046102.
63. Pereira, N., et al., *Ionic Liquid-Enhanced 3D Printed Flexible Resin for Pressure-Sensing Applications.* Advanced Materials Technologies, 2026. **11**(4): p. e01516.
64. Cruz, B.D.D., et al., *Ionic liquid–cellulose acetate composites as humidity sensors for agriculture 4.0 and related technologies.* Sustainable Materials and Technologies, 2026. **47**: p. e01818.

View Article Online
DOI: 10.1039/D6TC00186F

The data that support the findings of this study are available from the corresponding author, Nelson Pereira upon reasonable request.